2008

Obstacle detection and spectral discrimination using multi-wavelength motionless wide angle laser scanning

Kaveh Sahba
Edith Cowan University

Kamal Alameh
Edith Cowan University

Clifton Smith
Edith Cowan University

Obstacle detection and spectral discrimination using multi-wavelength motionless wide angle laser scanning

Kaveh Sahba[1], Kamal E. Alameh[1], and Clifton L. Smith[2]

WA Centre of Excellence for MicroPhotonic Systems, Electronic Science Research Institute, Edith Cowan University, 100 Joondalup Drive, Joondalup 6027, Western Australia
[2]School of Engineering and Mathematics, Edith Cowan University, 100 Joondalup Drive, Joondalup 6027, Western Australia
k.sahba@ecu.edu.au, k.alameh@ecu.edu.au, clifton.smith@ecu.edu.au; http://comps.ecu.edu.au

Abstract: Static laser scanning over a wide angle is demonstrated by ranging to 20 laser beams generated by a novel cylindrical quasi-cavity waveguide, using laser triangulation. Baseline distances and outgoing angles unique to each laser beam are calculated by modelling the triangulation arrangement using a system of linear equations and plotting principal rays. The quasi-cavity waveguide, imaging lens and focal plane are also plotted. The system is calibrated by finding optimal values for uncertain instrumental parameters using constrained non-linear optimization. Distances calculated over 5m indoors result in accuracies above 93%. Discrete laser spectroscopy using 640nm and 785nm laser diodes is also demonstrated. Both injected laser beams follow the same optical path through the quasi-cavity waveguide, enabling spectral measurements to be made from the same point on an object for both wavelengths. The reflected red and infrared laser light is digitally recorded by a CCD imager and differences in reflected intensity enable discrimination between various natural objects. This provides more complete information about the perturbing object, including its 3D coordinates as well as limited identification of its surface material.

OCIS codes: (300.6360) Spectroscopy, laser; (120.0280) Remote sensing and sensors; (150.3045) Industrial optical metrology; (280.3420) Laser sensors; (080.1510) Propagation methods

References and links

1. K. Sahba, K. E. Alameh, C. L. Smith, and A. Paap, "Cylindrical quasi-cavity waveguide for static wide angle pattern projection," Opt. Express **15**, 6 (2007).
2. L. F. Marshall, *Handbook of Optical and Laser Scanning* (Marcel Dekker Inc., 2004), Chap. 4.
3. A. B. Colquhoun, D. W. Cowan, and J. Shepherd, "Trade-offs in rotary mirror scanner design," Proc. SPIE **1454**, 12–19 (1991).
4. H. Horikawa, M. Miura, and T. Uchida, "Relationship between jitter and deformation of mirrors," Proc. SPIE **1454**, 20–32 (1991).
5. M. Hartrumpf and R. Munser, "Optical three-dimensional measurements by radially symmetric structured light projection," Appl. Opt. **36**, 13 (1997), http://www.opticsinfobase.org/abstract.cfm?URI=ao-36-13-2923.
6. K. Sahba, S. Askraba, and K. E. Alameh., "Non-contact laser spectroscopy for plant discrimination in terrestrial crop spraying," Opt. Express **14**, 25 (2006).
7. B. R. Myneni, F. G. Hall, J. P. Sellers, and A. L. Marshak, "The interpretation of spectral vegetation indexes," IEEE Trans. Geosci. Remote Sens. **33**, 2 (1995).
8. R. B. Fisher and D. K. Naidu, "A Comparison of Algorithms for Subpixel Peak Detection," Sanz, ed., in *Advances in Image Processing, Multimedia and Machine Vision* (Springer-Verlag, 1996).

#93471 - $15.00 USD Received 7 Mar 2008; revised 6 Apr 2008; accepted 6 Apr 2008; published 10 Apr 2008

1. Introduction

A new approach to generate laser beams over a wide angle demonstrates that the deflection function of a laser scanner can be achieved with no moving parts using a quasi-cylindrical optical cavity as a waveguide [1]. When an incident laser beam enters the cavity and undergoes multiple reflections, an array of beams is generated in accordance with the transmission coefficient of the thin film coating applied to the outer surface of the cavity. This approach is more robust and reliable when compared to the light deflection methods used in the current laser scanners deployed for perimeter security. These deflection methods are based on the rotation and oscillation of mirrors and/or optical heads at very high speeds, making the scanner prone to a variety of mechanical-related problems such as angular deviation from the intended optical path, jitter, synchronization issues, windage and most adversely, wear and tear [2-4].

This paper describes and demonstrates ranging to laser spots produced by a quasi-cylindrical optical cavity using wavelength division multiplexing in conjunction with active triangulation, thus producing 3D contour scanning of the surroundings. Since multiple beams are generated using the quasi cavity, ray propagation modelling using linear algebra is demonstrated and applied to predict the unique baseline location and bearing of every outgoing beam in the arrangement. The concept is demonstrated experimentally by adding the quasi-cylindrical optical cavity to a conventional active laser triangulation layout, imaging each spot with a CCD imager and a TV lens and implementing an appropriate Gaussian peak finder algorithm.

Multi-wavelength laser scanning using holographic diffraction grating methods is impractical because each laser beam would diffract at a specific angle according to its wavelength, making beam overlapping and alignment impossible. The key advantage of using the quasi-cavity waveguide is demonstrated as two laser diodes of different wavelengths follow the same optical path through the waveguide, enabling reflectance measurements to be made from the same point on an object surface. This feature is used to discriminate 8 sample objects into 3 classes based on differences in spectral responses.

2. Methodology

2.1 Ray modelling of the novel triangulation system

In a single laser spot triangulation arrangement, an imaging device of focal length f is positioned in line with the Z-axis and has the X-axis running through its lens centre. To the left of the lens, at a baseline distance β, a laser source launches a light beam at a variable angle w, as shown in Fig. 1.

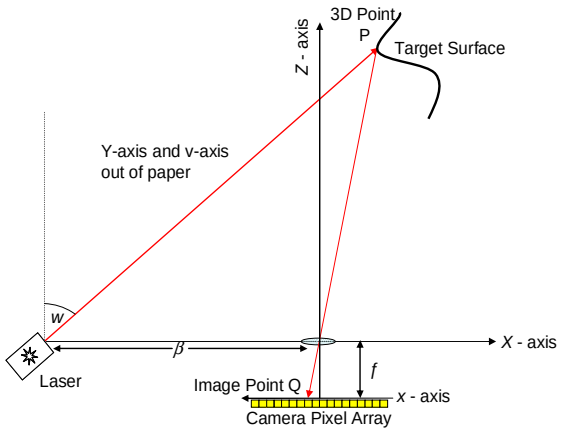

Fig. 1. Basic principle of active laser triangulation.

#93471 - $15.00 USD Received 7 Mar 2008; revised 6 Apr 2008; accepted 6 Apr 2008; published 10 Apr 2008

The image point lying on the *x*-axis, together with β, *w* and *f* determine the *X* and *Z* coordinates of the illuminated target point *P*. The distance *Z*, from the projected laser spot to the lens center is calculated by [5]:

$$Z = f \cdot \frac{x - \beta}{x - f \tan(w)}. \tag{1}$$

Figure 2 illustrates principal rays of the novel triangulation system incorporating the quasi-cylindrical optical cavity. Cavity interfaces and rays are plotted using equations for circles and straight lines, respectively. Figure 2 indicates that each outgoing laser beam has unique β and *w* values in relation to the rotated lens line, *L*. Note that Fig. 2 is to scale and represents the actual experimental setup.

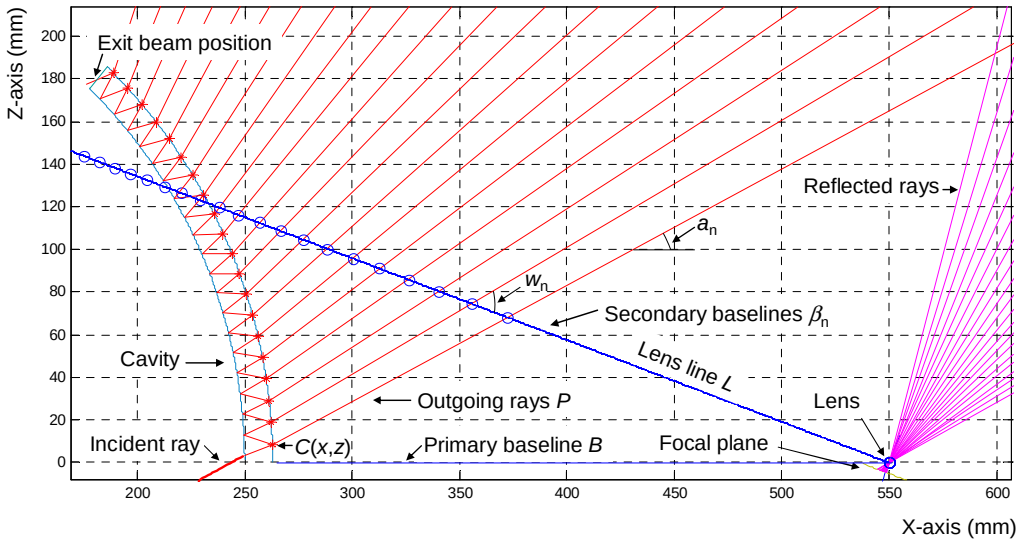

Fig. 2. Principal ray plot of the arrangement, showing outgoing and reflected rays, baselines, the quasi-cavity, lens and focal plane.

In calculating α_n, it was found that relying on the law of reflection and Snell's law produced theoretically correct values but did not predict the real angles. This could be attributed to several factors, namely, a non-homogeneous cavity substrate, an imperfect cylindrical shape or non-uniform dielectric thin film coatings. To derive accurate a_n values, the laser incident angle and cavity index defined in the model were altered so the exit beam position, shown in Fig. 2, coincided with the real point of exit at the end of the cavity, within 1mm accuracy. For any outgoing ray, the predicted coordinates of beam intersection with the outer cavity surface, $C(x,z)$ were recorded. The coordinates $S(x,z)$ of the corresponding laser spot on the laboratory wall were recorded manually by hand. In this case, the angle of a ray with respect to the *X*-axis is given by:

$$a = \tan^{-1}\left(\frac{C(z) - S(z)}{C(x) - S(x)}\right). \tag{3}$$

Each ray's outgoing angle with respect to the lens line of slope L_m is:

#93471 - $15.00 USD Received 7 Mar 2008; revised 6 Apr 2008; accepted 6 Apr 2008; published 10 Apr 2008

$$w = \tan^{-1}\left(\frac{a - L_m}{1 + (L_m \cdot a)}\right). \tag{4}$$

The baseline distance, β is calculated as:

$$\beta = \sqrt{(\beta(x) - L(x)) + (\beta(z) - L(z))}, \tag{5}$$

where

$$\beta(x) = \frac{L_b - P_b}{P_m + L_m}, \tag{6}$$

and

$$\beta(y) = \frac{(P_m \cdot L_b) - (L_m \cdot P_b)}{P_m \cdot L_m}. \tag{7}$$

P_m, L_m and P_b, L_b are the slope and y-intercept of a projected ray and the lens line, respectively.

2.2 Multi-wavelength object discrimination method

The first step in the object discrimination method is to determine the maximum recorded 12-bit digital intensity of the laser spot in digital numbers (d.n), $R(\lambda_n)$, where λ_n is the wavelength of the emitted laser beam. This is achieved by applying three-parameter, non-normalized Gaussian curve fitting to the one-dimensional intensity profile of the laser spot image. The intensity profile is defined by a row of pixels crossing the middle of the laser spot, along the *x*-axis. The Gaussian function of the fitted curve is defined as:

$$f(x) = a \cdot e^{-\frac{(x-b)^2}{2\cdot\sigma^2}}, \tag{8}$$

where a, b and σ are the maximum value, maximum position and standard deviation, respectively. After fitting this Gaussian curve, $R(\lambda_n) = a$ and is expressed in digital numbers on a scale according to the image sensor's bit depth.

The first discrimination factor is the gradient in recorded digital intensity, S, between any two (j,k) of the multiple wavelengths used. This approach has already been successfully validated for short range vegetation discrimination [6]. The slope value, S, is defined as:

$$S = \frac{R(\lambda_k) - R(\lambda_j)}{\lambda_k - \lambda_j}, \tag{9}$$

A secondary discriminating factor, the normalized difference index (*NDI*) is also used. It is defined as:

$$NDI = \frac{R(\lambda_k) - R(\lambda_j)}{R(\lambda_k) + R(\lambda_j)}. \tag{10}$$

#93471 - $15.00 USD Received 7 Mar 2008; revised 6 Apr 2008; accepted 6 Apr 2008; published 10 Apr 2008

NDI and *S* values are expressed in arbitrary units (a.u). *NDI* is especially useful when objects of interest absorb solar radiation around λ_j, but reflect and transmit solar radiation in the spectral region around λ_k [7].

3. Experimental setup

3.1 Experimental set up for triangulation using the quasi-cavity

The quasi-cavity is added to the conventional arrangement as shown in Fig. 2. It has a 45° curvature and generates 20 spots when an incident beam is injected through the entrance window. The number of outgoing beams depends on the laser position and incident angle. The cavity's orientation and position is set using a tilt and X-Y translation stage, respectively.

The incident beam is produced by a 632.3nm, 1mW, HeNe laser. This is mounted onto a rotating stage with 1° graduations. To image the projected laser spots, a ½" interline transfer CCD imager is employed, containing 768(H) × 494(V) pixels of size 8.4 × 9.8μm. A C-mount TV lens of focal length f = 12.5mm, collects the reflected laser light. The lens iris was adjusted appropriately to avoid saturation of the imaged spot. Images from the camera are digitized in 12-bit form using a Spiricon Plug and Play PCI frame grabber.

Both the quasi-cavity and camera were staged on a common rail, the distance between them defining the primary baseline, B = 0.3m. The arrangement is shown in Fig. 3.

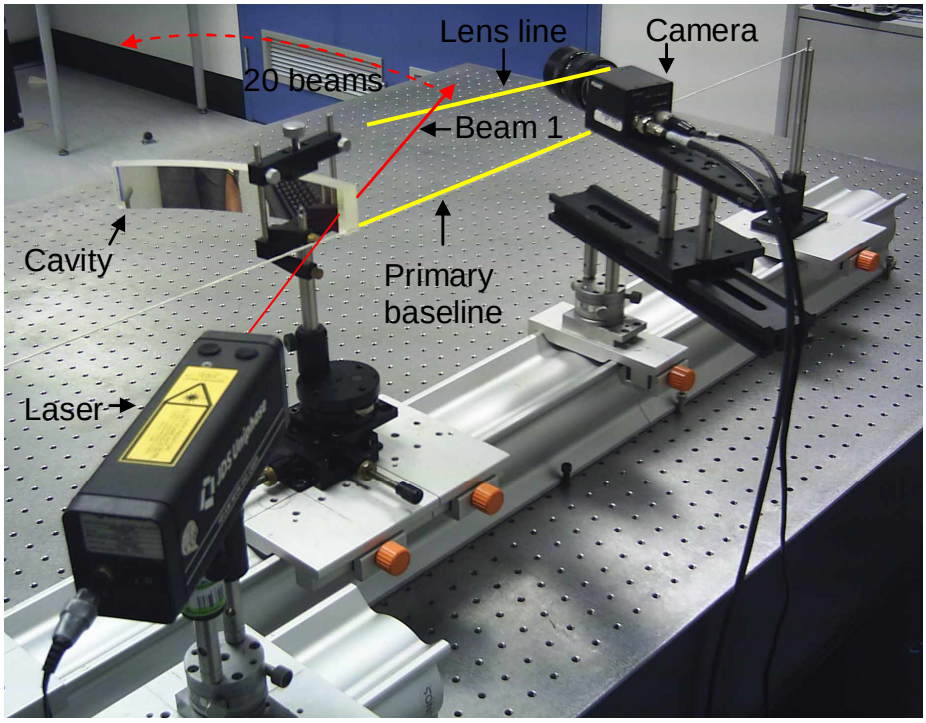

Fig. 3. Experimental setup for active triangulation using the quasi-cavity.

Two sets of range measurements were taken to validate the system. Firstly, all the laser spots were projected onto the laboratory walls and imaged. Since the field of view (FOV) of the camera lens is not wide enough to capture all spots instantaneously, the camera was rotated about the lens center in order to acquire two images containing 9 and 11 laser spots, which are shown in Fig. 4(a). The camera angle, L_θ, was set at 46º and 69º for images 1(a) and 1(b) respectively, with respect to the X-axis.

#93471 - $15.00 USD Received 7 Mar 2008; revised 6 Apr 2008; accepted 6 Apr 2008; published 10 Apr 2008

For the second set, a screen was placed 2.5m away from the camera lens centre. Thus spots 17 to 20 were projected onto the screen and the remainders were projected onto the wall. One image was taken of spots 12 to 20 to demonstrate that a closer object's range, with respect to the wall, could be accurately determined. L_θ, was set at 64.5°. The image is shown in Fig. 4(b).

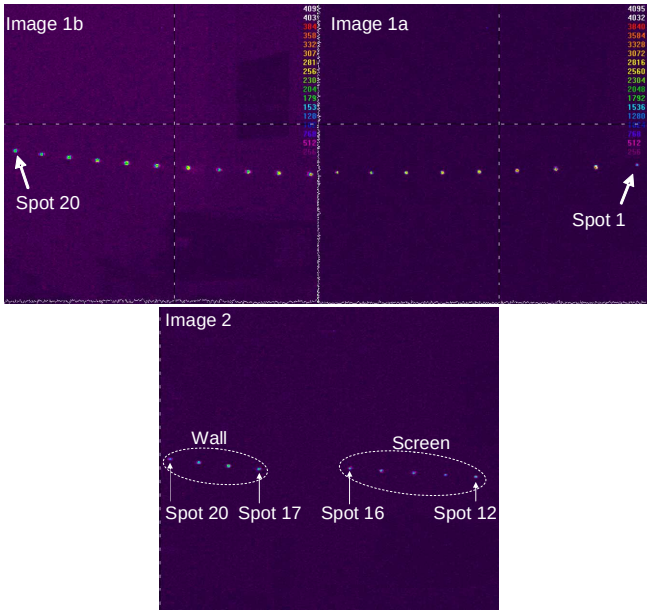

(a) (b)

Fig. 4. The laser spot array produced by the quasi-cavity where (a) shows all 20 laser spots projected onto the perimeter and (b) shows spots 12-1.

For each image, an intensity profile was taken across every spot and the digital pixel array processed to find the peak intensity pixel position using the Gaussian sub-pixel peak position estimator algorithm defined as [8]:

$$\hat{\delta} = \frac{1}{2}\frac{\ln(f(x-1)) - \ln(f(x+1))}{\ln(f(x-1)) - 2\cdot\ln(f(x)) + \ln(f(x+1))}, \tag{11}$$

where x is the pixel position of the observed peak sensor reading with an intensity of $f(x)$. The real peak position is at pixel $x + \delta$. Since the accuracy of δ depends on the imaged laser spots falling within the camera's depth-of-field (DOF), it was ensured that the laser spots were in focus, by appropriately adjusting the focal length and iris of the camera.

To calibrate the system, constrained nonlinear optimization was used to find the optimal values of parameters subject to uncertainties. The optimization was based on the minimization of the least square error, namely:

$$\sum \left(Z_i - \hat{Z}_i\right)^2, \tag{12}$$

where Z_i is the actual range and $\hat{Z}_i$ is the calculated range for the i^{th} laser spot. For the second set of ranges in Image 2, i = 12, since only spots 12 to 20 were imaged. The two most significant uncertainties in the experimental setup were:

#93471 - $15.00 USD Received 7 Mar 2008; revised 6 Apr 2008; accepted 6 Apr 2008; published 10 Apr 2008

1. Imager pixel size. Although already manufacturer-specified, the pixel pitch was not precisely known, thus producing error in calculating the captured ray's physical position on the image sensor. Hence, a pixel scaling factor, η, was used in modelling the pixel size.
2. L_θ is not totally accurate since the camera's rotating stage was fastened onto the sliding rail using a single bolt, hence making it subject to rotational movement due to slight knocks or vibrations.

Other uncertainties included the exact position of the lens centre along the optical axis within the complex TV lens system and the centre-to-centre alignment of the image sensor and lens. An alignment error attributed to the primary baseline, *B*, running directly through the lens centre could also have existed. Note that if the camera was displaced vertically, the lens would not be in the same plane as *B*, leading to inaccuracy in range measurements.

3.2 Experimental set up for multi-wavelength object discrimination

In the second part of this experiment, the same point on the remote target's surface was sequentially illuminated by two laser diodes of varying wavelengths, arranged with an optical beam combiner as shown in Fig. 5. This laser beam combination module replaced the HeNe laser used in the previous setup for triangulation as described in Section 3.1. All other aspects of the arrangement remained the same.

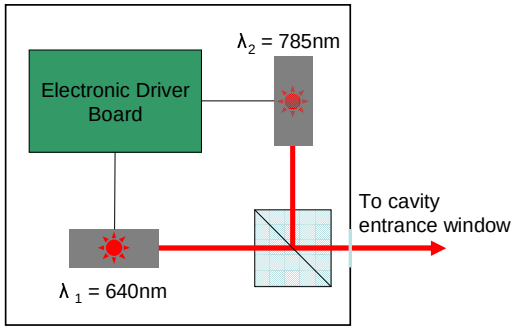

Fig. 5. Laser beam combination module.

The output beam diameter of each diode was 4mm. The combined beams propagate from the module through a single aperture as shown in Fig. 5. The laser diode sequencing was controlled by an eight channel digital output device interfaced to a computer via a universal serial bus interface (USB). The sequencing frequency and the optical output power of each diode was controlled by the laser driver trim-pot. The optical output power was set to 6mW.

The chosen sample objects were tree bark, wood, brick, soil, two green plants, black polyester fabric and aluminum. These objects were selected because they are commonly found indoors and outdoors. Black fabric was also chosen as it would be likely worn by an intruder within a perimeter security context. These samples were arranged so that one laser spot within the camera's FOV would fall on each object. After the desired wavelength was emitted, the camera grabbed a single frame containing the intensity profile of the spot array falling on the sample object under inspection. The intensity profile was then processed to produce *S* and *NDI* values for every object as explained in Section 2.2.

#93471 - $15.00 USD Received 7 Mar 2008; revised 6 Apr 2008; accepted 6 Apr 2008; published 10 Apr 2008

4. Experimental results and discussion

4.1 Laser triangulation results

Four frames were taken at each L_θ angle and the mean forward range, Z, to every spot obtained as shown in Fig. 6. The first set of estimated range measurements, for spots 1 to 20 projected on the laboratory walls, is shown in Fig. 6(a). The second set, from spots 12 to 20, is shown in Fig. 6(b).

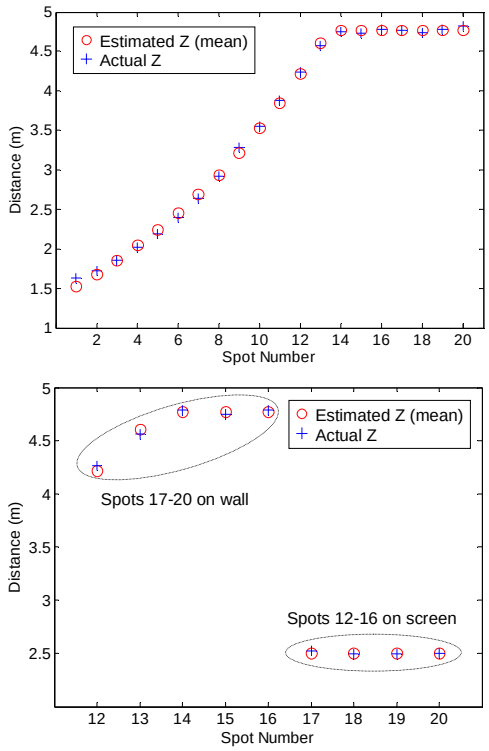

(a) (b)

Fig. 6. Mean estimated distance measurement results. (a) shows the mean estimated forward range, Z, for 20 laser spots falling on the laboratory walls. (b) shows the mean estimated forward range, Z, for spots 12 to 16 projected onto the walls and spots 17-20 onto a perturbing screen.

Note that Fig. 6 shows very good agreement between the measured and calculated ranges, validating the method of deriving β and w using linear algebra as described in previously. The minimum ranging accuracies achieved were 93.63% and 98.81% for spot 1 of measurement set 1 and spot 12 of measurement set 2, respectively. Standard deviation of the mean Z for every laser spot range measurement remained below 7.68cm and 0.525cm for measurement sets 1 and 2 respectively, demonstrating system stability in terms of repeatability.

Table 1 shows estimated and optimized η and L_θ values using constrained nonlinear optimization.

#93471 - $15.00 USD Received 7 Mar 2008; revised 6 Apr 2008; accepted 6 Apr 2008; published 10 Apr 2008

Table 1. Optimized values for pixel scale factor η and camera rotation angle L_θ.

	Image 1a		Image 1b		Image 2	
	η	L_θ	η	L_θ	η	L_θ
Estimate	1	46	1	72.5	1	68.5
Optimal	0.7744	50.107	0.9944	72.974	0.9825	69.507

4.2 Object discrimination results

According to the calculated *S* and *NDI* values, the sample objects can be clearly discriminated into 3 groups. The bark, wood, brick and soil samples display slope and *NDI* values of less than zero. The black polyester and aluminum values were also negative but there was a significant difference between the slope and *NDI* values. The Spathiphyllum and Anthurium green plant slope and *NDI* values are between 0.4 and 0.8, respectively, this clearly distinguishing them from the other samples objects. The slope and *NDI* values are shown in Fig. 7. Standard deviation of both the mean slope and *NDI* values for every sample object remained under 0.17 a.u.

The demonstrated object discrimination takes advantage of the fact that laser light of multiple wavelengths can be injected into the cavity and follow the same optical path, thus striking the same point on the object surface.

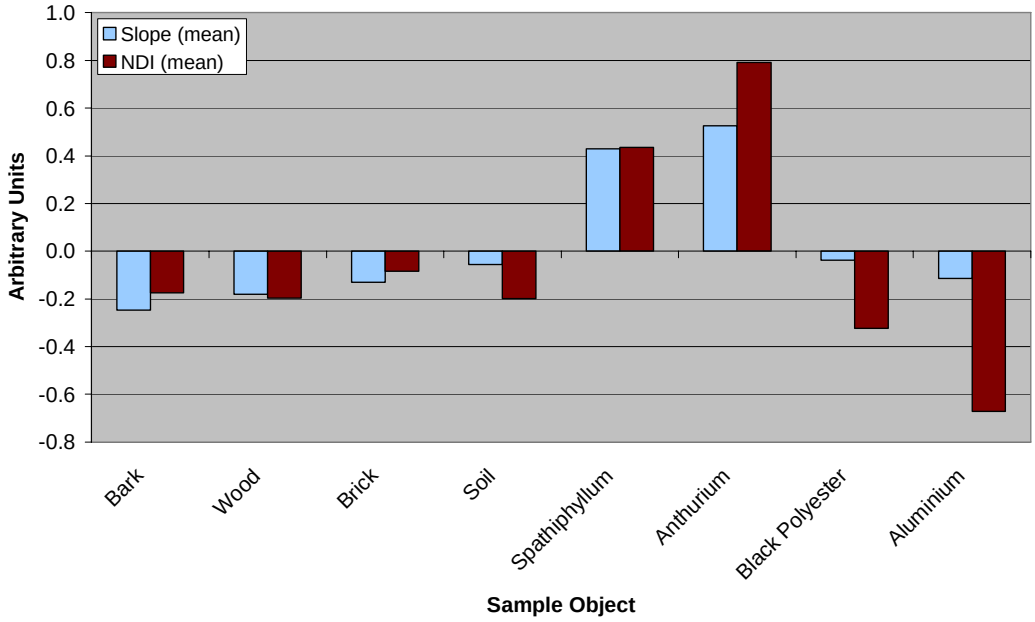

Fig. 7. Calculated *S* and *NDI* values.

Although in this case two wavelengths were used, the beam combination architecture could be expanded to combine more laser sources of varying wavelengths propagating the same optical path through the cavity. This is possible since the thin film coatings on the cavity rear and front interfaces have consistent transmission and reflection coefficients for wavelengths between 600 – 900nm. By combining more laser diodes emitting in this spectral

#93471 - $15.00 USD Received 7 Mar 2008; revised 6 Apr 2008; accepted 6 Apr 2008; published 10 Apr 2008

region, more slope and *NDI* values can be used to for more accurate discrimination between larger varieties of objects.

4. Conclusion

Range measurements to multiple laser spots generated over a wide angle by a novel waveguide component have been made with over 93% accuracy. A system of linear equations has been used to simulate the principal rays and components of the triangulation system and obtain the unique baseline distance and outgoing angle of every beam. Moreover, the imaging device can be rotated about its lens centre in order to triangulate to a spot array wider than its instantaneous FOV. Range accuracy is heavily dependent on the precise system arrangement, in terms of opto-mechanical instrumentation and experimental component placement and fastening. Calibration is achieved by non-linearly optimizing values for uncertain instrumental parameters.

Various objects have been illuminated with an array of collimated laser beams generated by the optical cavity. By digitally acquiring the reflectance data using two wavelengths and calculating spectral slope and *NDI* values for each object, limited object discrimination has also been demonstrated. The laser beam combination module architecture can easily be expanded by adding more wavelengths, thus improving the discrimination accuracy.

The active scanned angle shown in this arrangement can easily be extended by increasing the curvature of the quasi-cavity to 180º and placing a second imaging device in symmetry with the first, capturing spots on the left half of the laser transmission field. With the absence of moving parts, this type of scanning is particularly useful where robustness and mean time between sensor failures is critical, such as perimeter security.

#93471 - $15.00 USD Received 7 Mar 2008; revised 6 Apr 2008; accepted 6 Apr 2008; published 10 Apr 2008